

# PROCEEDINGS OF SPIE

[SPIDigitalLibrary.org/conference-proceedings-of-spie](https://spiedigitallibrary.org/conference-proceedings-of-spie)

## Simulation of experiments with partially coherent x-rays using Synchrotron Radiation Workshop

Oleg Chubar  
Maksim Rakitin  
Yu-Chen Chen-Wiegart  
Andrei Fluerasu  
Lutz Wiegart

# Simulation of experiments with partially-coherent X-rays using “Synchrotron Radiation Workshop”

Oleg Chubar<sup>\*a</sup>, Maksim Rakitin<sup>a</sup>, Yu-Chen Karen Chen-Wiegart<sup>a</sup>, Andrei Fluerașu<sup>a</sup>, Lutz Wiegart<sup>a</sup>

<sup>a</sup>National Synchrotron Light Source II, Brookhaven National Laboratory, NY, USA 11973

## ABSTRACT

High-accuracy physical optics calculation methods used in the “Synchrotron Radiation Workshop” (SRW) allow for multiple applications of this code in different areas, covering development, commissioning, diagnostics and operation of X-ray instruments at light source facilities. This presentation focuses on the application of the SRW code for the simulation of experiments at these facilities. The most complete and most detailed simulation of experiments with SRW is possible in the area of elastic coherent scattering, where the interaction of radiation with samples can be described with the same transmission-type “propagators” that are used for the simulation of fully- and partially-coherent radiation propagation through X-ray optical elements of beamlines. A complete “source-to-detector” simulation of such an experiment for a lithographic sample is described here together with comparisons of the simulated coherent scattering data with actual measurements results, obtained at the Coherent Hard X-ray (CHX) beamline of the National Synchrotron Light Source II (NSLS-II). Particular attention is paid to the analysis of visibility of speckles and intensity levels in the scattered radiation patterns at different degrees of coherence of the radiation entering the sample.

**Keywords:** synchrotron radiation, X-rays, physical optics, partial coherence, coherent scattering, computer simulations

## 1. INTRODUCTION

Complete, “source-to-detector”, simulations of experiments at light source facilities have a large number of benefits. Such simulations can allow for an accurate estimation of the feasibility of a given experiment, with a given sample, with a required resolution, at a particular beamline. This can be particularly important for new types of samples that are considered to be used in known types of experiments, and / or possibly for the development of new experimental schemes or even new types of experiments. The simulations can greatly help to determine optimal source and X-ray optics settings for a given experiment with a given sample (undulator gap and crystal angles, slit sizes, mirror radii of curvature, CRL configurations, etc.), determine optimal detector location, estimate expected radiation intensity distribution at the detector, required exposure time for a single measurement, duration of the entire experiment, etc. This can help to reduce the number of miscellaneous auxiliary measurements during experiment preparation and save expensive beam time. We note that such optimizations of beamline settings are particularly important for the experiments exploiting radiation coherence at modern storage ring based light sources, where, because of partial coherence of the generated radiation, a compromise between degree of radiation coherence (that typically determines resolution) and flux at the sample has usually to be done. Simulation of experiments can help to develop, test and tune experimental data processing algorithms, using simulated data, long before actual measurements. After the experiment, simulations can help to interpret the obtained experimental results more accurately. Simulations can also help to analyze impacts on quality of experimental data from miscellaneous electron beam and X-ray optics instabilities and other imperfections that may take place in a beamline, and to develop best strategies and priorities for their reduction or elimination.

Accurate simulation of emission and propagation of fully- and partially-coherent X-ray range Synchrotron Radiation (SR) through optical elements and drift spaces to a sample, using the SRW code [1] is currently done routinely for X-ray beamlines at NSLS-II [2] - [10]. The code uses Fourier optics and compatible methods for the simulation of fully-coherent radiation propagation, and it simulates partially-coherent radiation propagation through beamlines of storage-ring based SR sources by “summing-up” results of propagation of the fully-coherent radiation emitted by different “macro-electrons” seeded over the electron beam phase space [4].

\*chubar@bnl.gov; phone 1 631 344-4525; fax 1 631 344-8189; www.bnl.gov

Besides the simulation of radiation propagation through X-ray optics, these calculation methods allow for an easy simulation of several important types of experiments with X-rays that are performed at light source facilities, such as coherent scattering / coherent diffractive imaging and high-resolution transmission microscopy. In these experiments, the propagation of fully-coherent radiation through a thin sample can be simulated by the multiplication of the radiation transverse electric field components by complex transmission function(s) that can modify amplitudes and phases of the field components. After the sample, the propagation of the transmitted electric field to a detector can be simulated using a near- or far-field drift space propagator (depending on type of scattering and detection geometry). These propagation “steps” can be added to the sequence of propagations through elements of X-ray optics and drift spaces of the beamline at which the experiment is performed. The partially-coherent radiation propagation can be also easily simulated for such “extended” beamline using the same method that is used for the propagation through a “normal” beamline (before / without sample). This simulation scheme can possibly be improved in terms of CPU efficiency, e.g. if multiple propagations of the radiation through different sample(s) and drift space to the detector are required.

In this paper, we describe simulation of a test experiment of coherent X-ray scattering from a lithographic test sample containing sub-100 nm size objects (mimicking a dilute colloidal solution), and compare the simulation results with the results of actual measurements performed at the CHX beamline of NSLS-II. The main goal of this comparison was to test the accuracy of SRW simulations of this type of partially-coherent X-ray scattering experiments.

## 2. EXPERIMENTAL SCHEME AND RADIATION CHARACTERISTICS AT SAMPLE

### 2.1 Optical layout of the Coherent Hard X-ray beamline at NSLS-II

The CHX beamline is one of the first undulator-based coherence-exploiting hard X-ray beamlines constructed at NSLS-II. The beamline is specialized in X-ray photon correlation spectroscopy and other experimental techniques using coherent X-ray scattering [3]. The standard optical layout of the CHX beamline, excluding the source, 20 mm period 3 m long In-Vacuum Undulator IVU20, is shown in figure 1 as a sequence of its main optical elements. The beamline contains a number of slits / apertures (S0 - S3) installed along the optical path with the goal of “filtering-out the coherent portion” of partially-coherent X-ray flux of the input undulator radiation and matching the X-ray beam and sample dimensions. The beamline also includes a flat Horizontally-Deflecting Mirror (HDM) for harmonic suppression and reduction of heat load on subsequent optical elements, vertically-deflecting Double-Crystal Monochromator (DCM), vertically-focusing Compound Refractive Lens (CRL), horizontally-focusing Kinoform Lens (KL) with a dedicated aperture (KLA) preceding it. This optical setup creates ~10 - 20  $\mu\text{m}$  Full Width at Half Maximum (FWHM) size radiation spot at the nominal position of sample ~48.7 m from the undulator center. It should be noted that during experiments, the beam waist in the horizontal and vertical planes is usually chosen (by CRL and KL settings) to be located before the sample, roughly at the longitudinal position of the S3 “beam cleaning” slit, ~48 m from the undulator center. The sample used in the experiments and simulations covered by this paper is described in section 3.1. A photon counting EIGER X 4M type detector (with 75  $\mu\text{m}$  pixel size and 2070 x 2167 pixel numbers in the horizontal and vertical directions) was located at ~16 m from the sample.

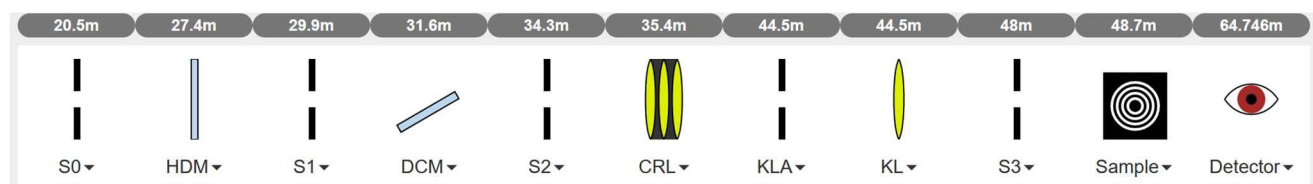


Figure 1. Experimental scheme at CHX beamline of NSLS-II generated by Sirepo GUI for SRW [11].

### 2.2 Calculated intensity distributions and degree of coherence of radiation at sample position

At NSLS-II, the coherent radiation flux represents only a portion of the total radiation flux emitted by undulators or other insertion devices. The optical design of the CHX beamline ensures transport of this flux portion to the sample and allows for easy modification of the degree of radiation coherence at the sample (in particular, in the horizontal plane). However, the degree of coherence can be increased at the expense of reduction of the radiation flux at the sample. This is illustrated by simulations presented in this section.

Horizontal and vertical cuts of the calculated intensity distributions and the degree of coherence of undulator radiation propagated through CHX beamline optics to the sample position, are shown in figure 2. The calculations were done using

the high-accuracy physical-optics methods implemented in the SRW code [4], for the beamline settings that were used in the actual measurements described in this paper. For these measurements and calculations, the photon energy was set to 9.65 keV (which is near the peak of the 5th harmonic of the IVU20 spectrum at  $\sim 6.7$  mm gap), and four different horizontal sizes of the S2 slit (see figure 1) were used: 30, 50, 100 and 200  $\mu\text{m}$ . For each of the horizontal S2 slit size values used, the horizontal size of the KLA was adjusted to “cut tails” of intensity distributions at the KL (the corresponding horizontal KLA sizes were respectively  $\sim 40$ , 60, 120 and 240  $\mu\text{m}$ ).

As one can see from the upper graphs in figure 2, the horizontal and vertical sizes of the intensity distributions are not strongly affected by changes of the horizontal S2 size: the horizontal FWHM spot size values vary between  $\sim 9.6$   $\mu\text{m}$  and  $\sim 13$   $\mu\text{m}$ , and the vertical FWHM spot size is  $\sim 9.7$   $\mu\text{m}$  in all cases. These values are in agreement with the results of actual measurements of the spot sizes at the sample position made in the scope of the experiments under discussion. The peak intensity and flux at the sample depend of course on the slit sizes: the spectral flux at 200  $\mu\text{m}$  horizontal S2 size is  $\sim 2.8 \times 10^{12}$  ph/s/.1%bw whereas in the case of 30  $\mu\text{m}$  S2 size it is only  $\sim 2.9 \times 10^{11}$  ph/s/.1%bw. These flux values, as well as the flux per unit surface values in the upper graphs in figure 2, take into account all known losses at optical elements along the beam path at CHX beamline (including the losses on slits / apertures installed after the S2 slit).

Even though the dimensions of the radiation spot at the sample do not vary strongly in the four cases simulated, the degree of coherence curves for the horizontal mid-plane (plotted vs half-difference of the horizontal conjugated coordinates,  $(x_1 - x_2)/2$ , see lower left graph in figure 2) strongly depend on the horizontal size of the S2 slit. The horizontal coherence length, estimated as FWHM size of a degree of coherence curve (central “lobe”), varies from  $\sim 20$   $\mu\text{m}$  at the 30  $\mu\text{m}$  horizontal S2 size down to  $\sim 2$   $\mu\text{m}$  at the 200  $\mu\text{m}$  horizontal S2 size, indicating that in the former case the radiation at sample is  $\sim$ fully coherent in the horizontal plane (since the coherence length is larger than the spot size), whereas in the latter case the coherence is rather low (the coherence length is much smaller than the spot size).

In the vertical plane, the coherence length is  $\sim 16$   $\mu\text{m}$ , and, as the vertical spot size, it does not depend on the horizontal S2 slit size (see lower-right graph in figure 2). Note that this coherence length value is larger than the  $\sim 9.7$   $\mu\text{m}$  vertical FWHM spot size, meaning that the radiation at sample is  $\sim$ fully coherent in the vertical plane.

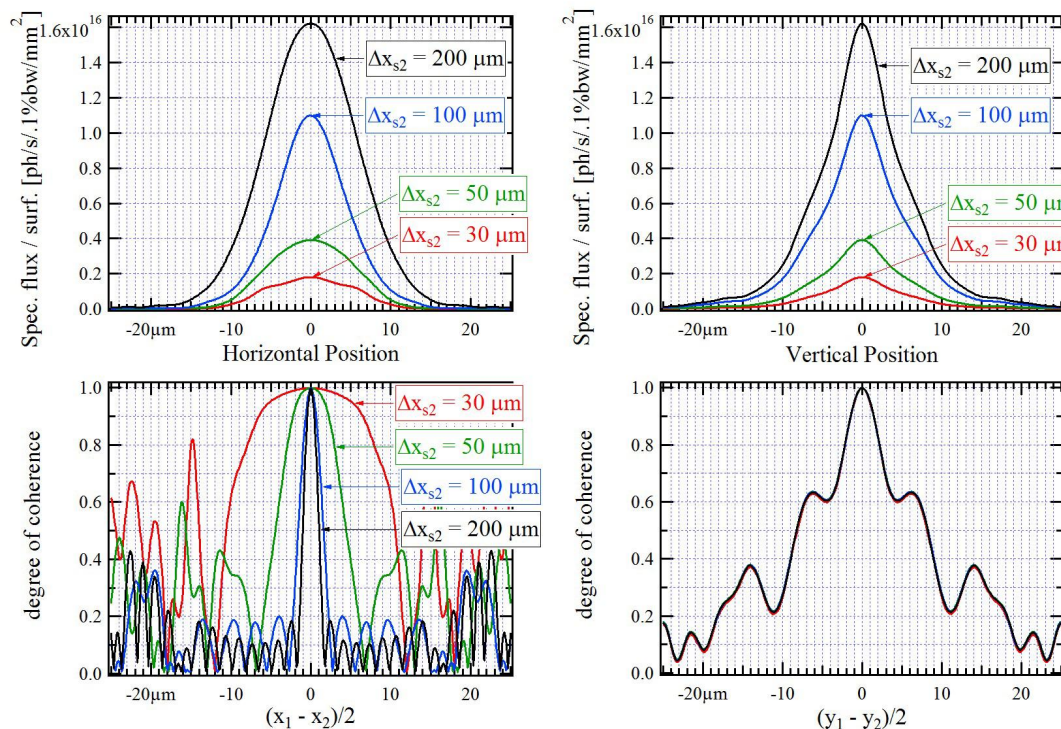


Figure 2. Horizontal and vertical mid-plane cuts of the X-ray beam intensity distributions (upper graphs) and the degree of coherence in the horizontal and vertical mid-planes (lower graphs) at sample position for four different horizontal S2 slit size values used at the experiments at CHX beamline.

### 3. COHERENT SCATTERING MEASUREMENTS AND SIMULATIONS

#### 3.1 Sample description and representation for SRW simulations

A sample was created by lithography-based techniques, at the Center for Functional Nanomaterials (CFN) of the Brookhaven National Laboratory (BNL) for miscellaneous commissioning / calibration type measurements at the CHX beamline. The sample includes a large number of Au nano-objects of nearly-rectangular shape (with  $\sim 65 \times 58$  nm average transverse dimensions and  $\sim 50$  nm thickness) randomly-distributed over a  $\sim 50 \times 50$   $\mu\text{m}$  area of a sub- $\mu\text{m}$  thickness silicon nitride ( $\text{Si}_2\text{N}_4$ ) membrane. A fragment of an Electron Microscope (EM) image of this sample is shown in figure 3 on the left.

For simulations with the SRW code, such a “thin” sample can be represented by a “transmission” type optical element that (in a general case) can modify amplitude and phase of the radiation electric field differently at different horizontal and vertical positions in a given transverse plane (where the sample is located). To facilitate the generation of SRW transmission objects directly from EM images of real samples, a special module has been added to the Python version of the SRW code. Functions of this module can convert an original EM image, saved in one of the popular graphical file formats, first to a simplified / transformed intermediate image, and then, with an eventual extra input (defining materials, thicknesses of objects in the sample plane, etc.), to a corresponding SRW Python object ready for use in simulations. A fragment of the intermediate image created from the EM image of the sample described above is shown on the right in figure 3. Besides the suppression of background and removal of parts of the original image that don’t directly represent the sample, a  $\sim 30^\circ$  rotation was applied to the intermediate image to represent orientation of the sample used in actual measurements at the beamline.

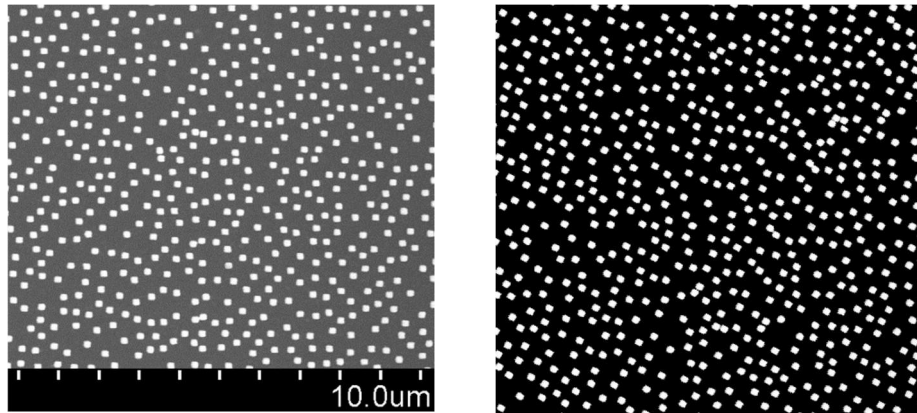


Figure 3. Original electron microscope image of the “random Au nano-dots” sample manufactured at the CFN / BNL (left) and the corresponding processed image used as input for definition of a complex transmission object for SRW simulations (right).

#### 3.2 Measured and simulated intensity distributions of scattered partially-coherent X-rays

The measured and calculated intensity distributions of X-rays at 9.65 keV photon energy scattered by the sample described in section 2.2 are presented in figures 4 and 5 on a logarithmic scale. Figure 4 shows typical 2D intensity distributions, measured by the EIGER detector (on the left) and simulated for the conditions of the measurements (on the right). The  $75 \mu\text{m} \times 75 \mu\text{m}$  detector pixel size was taken into account in the simulations: intensity distributions on a denser mesh with  $\sim 15 \mu\text{m}$  step size in both directions were initially produced by the radiation propagation simulations, and then these distributions were processed (integrated within pixel dimensions for different pixel locations over the horizontal and vertical position) to generate the final distributions to be compared with the measured ones. The white horizontal and vertical lines passing through  $\sim$ centers of the measured and calculated distributions result from diffraction of X-rays at the last slit (S3) before the sample (see figure 1). The horizontal and vertical size of this slit was set to  $30 \mu\text{m}$  during the measurements, which was larger than the FWHM beam size at the location of the S3 slit; however, despite this, the slit diffraction nevertheless caused a considerable contribution, well visible in the log-scale, both to the measured and the calculated intensity distributions. The black lines in the measured intensity distribution correspond to the X-ray “beam stop” and gaps between the detector modules. Besides the presence of these lines in the measured image plot, the two images look remarkably similar. The concentric pattern well seen in both images results from scattering of the radiation at



each sub-100 nm nearly-rectangular shape Au object of the sample (form factor). We note that both in the measurements and in the simulations the sample was rotated by  $\sim 30^\circ$  with respect to its nominal orientation (when the sides of the  $\sim$ rectangular objects are parallel to the horizontal and vertical directions in the laboratory frame). Such orientation of the sample allowed to obtain strong minima and maxima of the main pattern along a line (shown by dashes in both images) that does not coincide with the slit-diffraction dominated horizontal and vertical lines passing through the image centers.

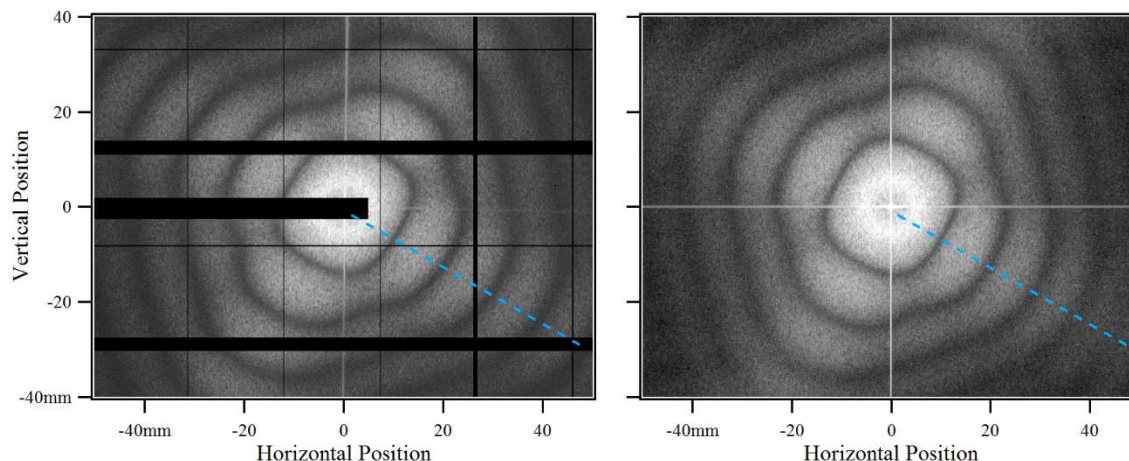


Figure 4. Measured (left) and calculated (right) logarithmic image plots of 2D intensity distributions (speckle patterns) of X-rays at 9.65 keV photon energy scattered by the sample illustrated in figure 3, for 50  $\mu\text{m}$  horizontal S2 slit size.

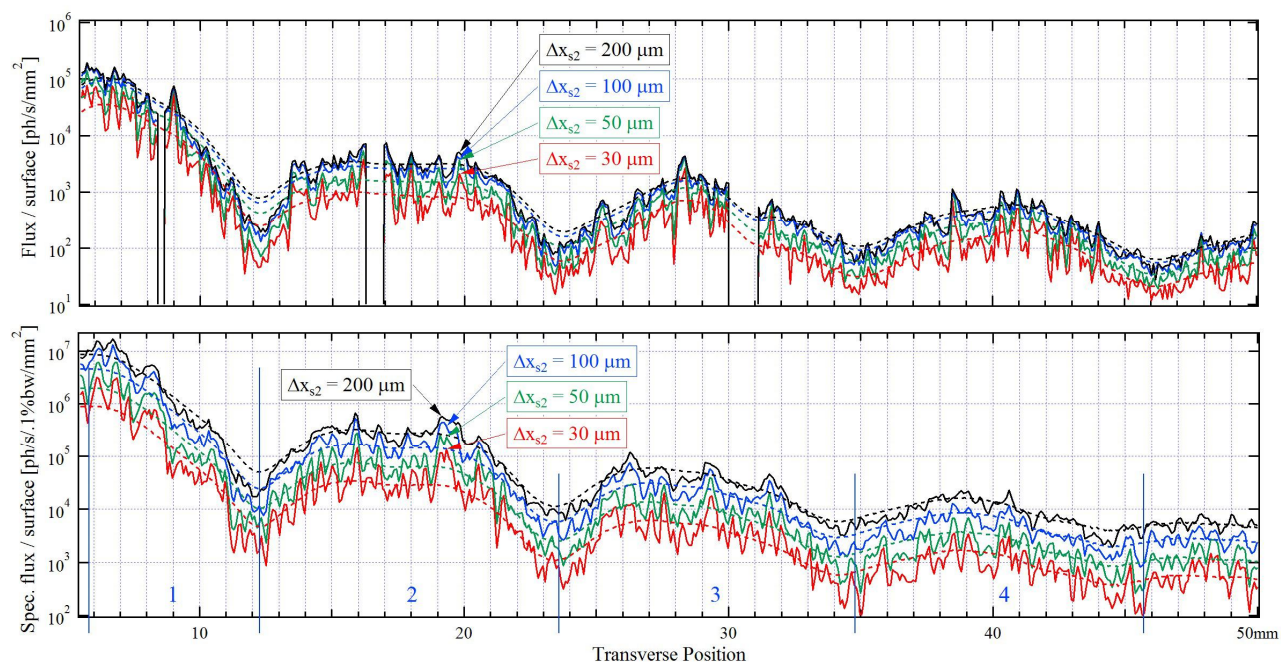


Figure 5. Cuts of intensity distributions (speckle patterns) of scattered X-rays along a segment of the dashed line shown in the image plots in figure 4: measured (top) and calculated (bottom) for different horizontal S2 slit sizes defining radiation coherence and flux at sample. Solid lines belong to the actually measured and calculated intensity distributions, dashed lines indicate the corresponding “smoothed-out” distributions containing no speckles. “Empty” intervals in the measured data correspond to gaps between detector modules.

The small light and dark “dots” filling the entire areas of both images in figure 4 represent “speckles” resulting from the interference of the (partially) coherent radiation scattered from different parts of the sample. Such speckle patterns contain information about the mutual locations of nano-objects in the sample, and therefore usually represent the main “value” in studies of mesoscopic structures using coherent X-ray scattering methods. For an accurate analysis, the visibility of speckles, or speckle contrast in the coherent scattering patterns, may need to be high enough. The speckle contrast strongly depends on the degree of coherence of the radiation illuminating samples. However, as this was illustrated in section 2.2, the higher is the degree of coherence the lower is the radiation flux at sample, and so the longer is a required exposure time for an individual measurement. Too long exposure times may limit temporal resolution in time-dependent measurements of non-static samples, and / or may integrate miscellaneous beam instabilities and impose other technical constraints to the measurements. Therefore, coherent scattering experiments at beamlines of storage ring based SR sources may require thorough optimization of beamline settings for finding a good compromise between the radiation coherence and flux, and such optimizations have to include simulation of the radiation scattering at samples.

The work presented in this paper included therefore measurements and simulations of coherent scattering from the same sample at different horizontal sizes of the S2 slit impacting the degree of coherence and flux at sample location. Measurements and simulations were performed for the same four values of the horizontal S2 size, for which the calculations of the intensity distributions and degree of coherence at sample were done (see section 2.2). The measured and simulated scattered radiation intensity distribution cuts made along a segment of the dashed line indicated in the image plots in figure 4 (passing at  $\sim 30^\circ$  angle with respect to the horizontal axis) are shown in figure 5. As one can see from the graphs in this figure, the lowest flux per unit surface area and the highest speckle contrast in the measured and calculated distributions correspond to the smallest, 30  $\mu\text{m}$ , horizontal S2 size, whereas the highest flux per unit surface area and lowest speckle contrast correspond to the largest, 200  $\mu\text{m}$ , S2 size. The smaller difference between the 100  $\mu\text{m}$  and 200  $\mu\text{m}$  S2 size cases in the measured data is likely to be explained by an effective KL (see figure 1) aperture that is limited to  $\sim 100 - 150 \mu\text{m}$  due to the etching quality of its external zones.

For a more quantitative characterization and comparison of the measured and calculated intensity distributions of the scattered radiation, we introduced the following approximate speckle contrast “figure of merit”:

$$\delta = \frac{1}{N} \sum_{j=1}^N \frac{[I(s_j) - \bar{I}(s_j)]^2}{[\bar{I}(s_j)]^2}, \quad (1)$$

where  $I(s)$  is the measured or calculated flux per unit surface area at  $s$  longitudinal position along certain line / cut of a 2D distribution, and  $\bar{I}(s)$  is the value of the corresponding “smoothed-out” flux distribution, that does not contain speckles, yet takes into account features of scattering from one (average) object / feature of the sample, at the same position  $s$ . The values of the two distributions are considered at an equidistant mesh vs  $s$ , with  $s_j$  ( $j = 1, 2, \dots, N$ ) corresponding to detector pixel center locations within a given interval. Eq. (1) represents an estimate of a relative “standard” (root-mean-square) deviation of an actual partially-coherent scattered radiation distribution (possibly containing speckles) from the corresponding “smoothed-out” (i.e. “incoherent”) radiation distribution containing no speckles. For the estimates in the scope of this paper, the “smoothing-out” of the actual intensity distributions was done using a convolution of the actual 2D distributions with a 2D Gaussian (normalized to 1) having the FWHM dimensions exceeding typical speckle sizes in the two transverse directions. The cuts of these distributions are shown by dashed lines in figure 5 graphs.

Table 1. Measured / simulated values of relative standard deviations of the intensity in speckle patterns from the corresponding averaged intensity distributions (estimated according to Eq. (1)), for four different intervals in the distributions and four different horizontal S2 slit sizes.

Horiz. S2 size [ $\mu\text{m}$ ]	Intensity distribution region			
	1	2	3	4
30	0.82 / 0.97	0.70 / 0.96	0.72 / 0.78	0.68 / 0.51
50	0.71 / 0.87	0.60 / 0.83	0.62 / 0.72	0.57 / 0.43
100	0.55 / 0.73	0.47 / 0.63	0.47 / 0.56	0.39 / 0.31
200	0.51 / 0.50	0.43 / 0.38	0.41 / 0.37	0.36 / 0.27

The values of  $\delta$  estimated according to Eq. (1) for four different intervals in the scattering patterns indicated in the lower graph in figure 5, for four different horizontal S2 slit sizes are presented in table 1. Each value before slash (“/”) in central part cells refers to a measured intensity distribution, and the value after slash refers to a corresponding calculated distribution. As one can clearly see from table 1, the speckle contrast, characterized by  $\delta$  according to Eq. (1), reduces with the increase of the horizontal S2 size in each of four intervals of the distributions, which is in agreement with the radiation degree of coherence calculations described in section 2.2. The total speckle contrast reduction between the cases of 30  $\mu\text{m}$  and 200  $\mu\text{m}$  is stronger in the simulations data compared to measurements, with the minimal contrast reduction taking place between the 100  $\mu\text{m}$  and 200  $\mu\text{m}$  S2 size cases. This can be explained by the same KL effective aperture issue that makes the measured flux difference small between these two cases (see upper graph in figure 5 and explanations above).

## 4. CONCLUSIONS

Detailed source-to-detector simulations of test coherent scattering experiments with an artificially-created lithographic sample containing a large number of sub-100 nm size objects were performed, using the SRW code, along with actual measurements at the CHX beamline of NSLS-II. A good general agreement between the measured and simulated scattering data was obtained in terms of speckle contrast and its dependence on the key beamline settings (slit sizes). This confirms the accuracy of the SRW calculations and suggests potential applicability of this code for more complicated simulations and related beamline settings optimization for coherent scattering experiments with different types of samples.

## ACKNOWLEDGMENTS

We would like to thank A. Stein, C. Black, K. Yager and B. Ocko for preparation of samples at CFN/BNL, and D. L. Bruhwiler, R. Nagler, P. Moeler (RadiaSoft) for collaboration on Sirepo and SRW development. The experiment simulation work was supported by US DOE contract DE-SC0012704 and SBIR grant DE-SC0011237.

## REFERENCES

- [1] Chubar, O. and Elleaume, P., “Accurate and efficient computation of synchrotron radiation in the near field region,” Proc. EPAC-98, 1177-1179 (1998).
- [2] Chubar, O., Chu, Y. S., Kaznatcheev, K., Yan, H., “Application of partially coherent wavefront propagation calculations for design of coherence-preserving synchrotron radiation beamlines,” Nucl. Instrum. and Methods A649 (1), 118-122 (2011).
- [3] Fluerasu, A., Chubar, O., Kaznatcheev, K., Baltser, J., Wiegart, L., Evans-Lutterodt, K., Carlucci-Dayton, M., Berman, L., “Analysis of the optical design of the NSLS-II coherent hard x-ray beamline,” Proc. SPIE 8141, 81410J (2011).
- [4] Chubar, O., Berman, L., Chu, Y. S., Fluerasu, A., Hulbert, S., Idir, M., Kaznatcheev, K., Shapiro, D., Shen, Q., Baltser, J., “Development of partially-coherent wavefront propagation simulation methods for 3rd and 4th generation synchrotron radiation sources,” Proc. SPIE 8141, 814107 (2011).
- [5] Chubar, O., Fluerasu, A., Berman, L., Kaznatcheev, K., Wiegart, L., “Wavefront propagation simulations for beamlines and experiments with Synchrotron Radiation Workshop,” Proc. SRI-2012, J. Phys.: Conf. Ser. 425, 162001 (2013).
- [6] Chubar, O., “Recent updates in the Synchrotron Radiation Workshop code, on-going developments, simulation activities, and plans for the future,” Proc. SPIE 9209, 920907 (2014).
- [7] Canestrari, N., Bisogni, V., Walter, A., Zhu, Y., Dvorak, J., Vescovo, E., Chubar, O., “Wavefront propagation simulations for a UV/soft X-ray beamline: Electron Spectro-Microscopy beamline at NSLS-II,” Proc. SPIE 9209, 92090I (2014).
- [8] Wiegart, L., Fluerasu, A., Bruhwiler, D. L., Chubar, O., “Partially coherent wavefront propagation simulations: mirror and monochromator crystal quality assessment,” Proc. SRI-2015, AIP Conf. Proc. 1741, 040013 (2016).
- [9] Wiegart, L., Rakitin, M., Fluerasu, A., Chubar, O., “X-ray optical simulations supporting advanced commissioning of the coherent hard X-ray beamline at NSLS-II,” these proceedings.
- [10] Williams, G., Robinson, I., Chubar, O., Berman, L., Chu, Y. S., “Optical design and simulation of a new coherence beamline at NSLS-II,” these proceedings.
- [11] Rakitin, M., Chubar, O., Moeller, P., Nagler, R., Bruhwiler, D. L., “Sirepo: a web-based interface for physical optics simulations – its deployment and use at NSLS-II,” these proceedings.